Sensors & Actuators: B. Chemical 352 (2022) 130962

Contents lists available at ScienceDirect

Sensors and Actuators: B. Chemical

journal homepage: www.elsevier.com/locate/snb

Characterizing a sensitive compact mid-infrared photoacoustic sensor for methane, ethane and acetylene detection considering changing ambient parameters and bulk composition (N_2, O_2 and H_2O)

Jonas Pangerl [a,b,*], Max Müller [a,b], Thomas Rück [a], Stefan Weigl [a], Rudolf Bierl [a]

[a] Sensorik-ApplikationsZentrum (SappZ) der Ostbayerischen Technischen Hochschule (OTH) Regensburg, 93053 Regensburg, Germany
[b] Institut für Analytische Chemie, Chemo und Biosensorik, Universität Regensburg, 93053 Regensburg, Germany

ARTICLE INFO

Keywords:
Methane
Ethane
Acetylene
Photoacoustic spectroscopy
Interband cascade laser
Cross-sensitivities
Relaxation effects

ABSTRACT

We present a sensitive and compact interband cascade laser (ICL) based photoacoustic setup for the detection of gaseous hydrocarbons and discuss its applicability towards trace gas analysis. We investigated the performance of the sensor for trace concentrations of methane, ethane and acetylene diluted in nitrogen. The excitation of methane and ethane was accomplished using one tunable diode laser, covering a range from 3360 to 3372 nm, which was replaced by a separate ICL at 3025 nm for acetylene detection. The influence of ambient parameters such as temperature, flow rate and pressure as well as potential cross-sensitivities towards O_2 and H_2O have been examined in terms of methane and acetylene detection. A series of simulations proved several of these influences to be attributed to relaxation effects. With a 3σ limit of detection (LoD) of 6.8 parts per billion (ppbV) in case of methane, 2.3 ppbV regarding ethane and 3.6 ppbV in terms of acetylene, the sensor demonstrates a great potential for applications in the field of trace gas analysis.

1. Introduction

Photoacoustic spectroscopy (PAS) is a well-known technique for trace gas analysis, which is used in a variety of applications, such as food safety [1–3], breath analysis [4–7] or environmental analysis [8–10] to name only a few. PAS is recognized for its high sensitivity and spectral selectivity as well as its miniaturization capabilities. Compared to conventional absorption spectroscopy (AS), PAS offers certain advantages, especially in the field of trace gas monitoring, although both principles are based on the absorption of light. For instance, trace gas concentrations in the two-digit parts per trillion (pptV) range have already been accomplished by means of PAS [9]. Besides, the possibility of applying low-cost components, e.g. cell phone microphone, 3D printed measuring cell etc., enhance the popularity of PAS. Moreover, compared to an optical sensor, the measurement time can be reduced to less than ten percent by using a microphone in PAS [11]. The photoacoustic effect is based on absorption of light causing ro-vibrational or ro-vibroic excitation of analyte molecules. When restoring the initial state after excitation, only non-radiative relaxation, more precisely a vibrational translational (VT) energy transfer, contributes to photoacoustic (PA) signal generation. This deactivation process is based on molecular collisions of excited analyte molecules with surrounding molecules. In detail, the internal energy stored due to absorption is transformed into translational (kinetic) energy of the surrounding molecules by inelastic collisions, which yields a local heat input that is represented by the heat production rate $\dot{H}$. As a consequence of sine-modulating the light source, alternating dilatation and contraction generate a periodic pressure oscillation, which in turn stimulates a standing acoustic wave as we utilize a cylindrical resonator for amplification reasons. This resulting sound wave can be detected as an acoustic signal with an amplitude that is directly proportional to the analyte concentration. In order to improve the signal-to-noise ratio (SNR) and to mitigate spectral cross-sensitivities, this work is based on wavelength modulation (WM) while the PA signal is measured at the second harmonic of the modulation frequency.

Our research focuses on the detection of low concentrated hydrocarbons, namely methane, ethane and acetylene. We identified the dissolved gas analysis (DGA) to be a future application for such a sensor, as these inflammable species are eluted from transformer oil during operation. If this degradation process is not detected at an early stage, this

* Corresponding author at: Sensorik-ApplikationsZentrum (SappZ) der Ostbayerischen Technischen Hochschule (OTH) Regensburg, 93053 Regensburg, Germany.
E-mail addresses: jonas2.pangerl@oth-regensburg.de (J. Pangerl), max.mueller@oth-regensburg.de (M. Müller), thomas.rueck@oth-regensburg.de (T. Rück), stefan.weigl@oth-regensburg.de (S. Weigl), rudolf.bierl@oth-regensburg.de (R. Bierl).

https://doi.org/10.1016/j.snb.2021.130962
Received 25 March 2021; Received in revised form 10 August 2021; Accepted 18 October 2021
Available online 21 October 2021

may lead to short circuits or even fire within the transformer. Furthermore, methane is one of the most important gases related with the greenhouse effect and contributes up to 9 % to global warming [12]. Besides, monitoring hydrocarbons is essential for a variety of applications in medical diagnostics, e.g. the analysis of exhaled human breath [4–7,13,14].

Literature provides several photoacoustic systems addressing the detection of hydrocarbons that report limits of detection (LoD) down to 65 pptV (1σ) for methane [15] and 25 pptV (3σ) for ethane [16] using a continuous wave (cw) optical parametric oscillator (OPO) laser system. In terms of acetylene a high-power Q-switched laser was used to reach an LoD of 101 pptV (3σ) [17]. The ICL-PAS system of Sampaolo et al. allowed for the detection of methane and ethane concentrations of 90 ppbV and 7 ppbV, respectively [18]. Zheng et al. achieved an LoD of 3.6 ppmV in terms of methane using an 3.2 μm interband cascade light emitting device (ICLED) [19] as well as an LoD of 600 pptV using a 3.3 μm ICL and an averaging time of 90 s [20]. Wu et al. accomplished a 1σ LoD of 50 ppbV CH_4 by means of a 3.3 μm DFB laser [21]. After averaging for 200 s and using a 1.5 μm DFB laser, Chen et al. achieved a 1σ LoD of 27 pptV C_2H_2, which to the best of the authors knowledge is the lowest value reported so far for photoacoustic acetylene detection [22].

However, these publications either base upon expensive high-power laser systems, bulky laboratory measurement setups or laboratory measuring conditions, i.e. they perform only minor or no real condition testing. In this work, we developed a highly sensitive and compact WM-PAS sensor for methane, ethane and acetylene detection by using only two ICLs emitting at around 3365 nm and 3025 nm with an output power of about 10 mW. Each laser diode is mounted into a TO66 housing with integrated optics and temperature control. The TO66 housing in turn is mounted into a 3D printed heat sink which is screwed onto a compact photoacoustic measurement cell (PAC). Previous investigations that revealed no cross-sensitivities in terms of spectral interference are not discussed within this work. Since H_2O is well known to absorb rather constantly in the wavelength ranges that are considered in this work, the technique of wavelength modulation was preferred against intensity modulation. However, we do provide a comprehensive analysis considering the impact of various ambient parameters like temperature, pressure and mass flow on the photoacoustic signal. Besides, we investigated potential non-spectral cross-sensitivities towards changes in the bulk composition, i.e. N_2, O_2 and H_2O, in detail. Furthermore, we performed a series of simulations based on a kinetic model, demonstrating that mainly relaxation effects are accountable for photoacoustic signal changes.

2. Derivation of the photoacoustic signal

Generally, at modulation frequencies in the kHz range, the time-dependent heat production rate related to molecular absorption at thermal equilibrium $\dot{H}(t)$ with unit $\mathrm{Js^{-1}m^{-3}}$ can be simplified to

$$\dot{H}(t) = \dot{H}_0 e^{i\omega t} \tag{1}$$

$$\dot{H}_0 = \rho\sigma(\tilde{\nu}_{\mathrm{Ph}})I_0 = \alpha I_0 \tag{2}$$

where ω is the modulation frequency, $\sigma(\tilde{\nu}_{\mathrm{Ph}})$ is the absorption cross-section in $\mathrm{m^2}$ per molecule at the wavenumber $\tilde{\nu}_{\mathrm{Ph}}$ and $\alpha = \rho\sigma(\tilde{\nu}_{\mathrm{Ph}})$ is the absorption coefficient of the analyte gas with unit $\mathrm{cm^{-1}}$, respectively. The molecular volume density ρ in molecules per $\mathrm{m^3}$ can be calculated via the dimensionless volume ratio N in ppmV times the ratio of Avogadro-constant N_A and molar volume V_{mol}, $\rho = NN_A V_{\mathrm{mol}}^{-1}$. I_0 corresponds to the incident light intensity in $\mathrm{Wm^{-2}}$, calculated by the product of photon flux Ψ_0 in $\mathrm{s^{-1}m^{-2}}$, Plank constant h, speed of light c_0 and the wavenumber:

$$I_0 = \Psi_0 \mathrm{h} c_0 \tilde{\nu}_{\mathrm{Ph}} \tag{3}$$

In terms of PAS, the absorption of a modulated light beam and the subsequent conversion into thermal energy causes the generation of a sound wave. By solving two coupled differential equations originating from six linear independent quantities (temperature, pressure, density of the gas and its three dimensional molecular velocity vector) for the sound pressure $p_a(\vec{r},\omega)$, a damped wave equation is obtained. Neglecting the loss term, which prevents an analytical solution and applying Fourier transformation on both sides yields an inhomogeneous Helmholtz-equation, linking the frequency-dependent heat production rate derived from the absorption of photons to the generation of an acoustic wave

$$\left(\Delta + \frac{\omega^2}{c_s^2}\right) p_a(\vec{r},\omega) = \left(\frac{\gamma - 1}{c_s^2}\right) i\omega\dot{H}(\vec{r},\omega) \tag{4}$$

Here, c_s is the speed of sound and γ is the heat capacity ratio. The solution of the neglected loss term directly depends on the geometry of the PAC. We use a tube-shaped two-side open resonator with a cylindrical buffer volume attached to each side. Therefore, the criterion for longitudinal resonance amplification is

$$L_R = k\frac{\lambda_s}{2} \tag{5}$$

with L_R being the resonator length and λ_s the wavelength of a standing soundwave of order k. By disregarding the node shifting effect, which prevents an analytical solution, according to [23] an expression for the photoacoustic pressure signal $p_a(\vec{r},\Omega_k)$ is found to be

$$p_a(\vec{r},\Omega_k) = (\gamma - 1)\frac{Q_k}{\Omega_k}\frac{L_R}{V_R}\alpha P_0 p_k e^{-\mu_k}\cdot p_k(\vec{r}) \tag{6}$$

Here, Ω_k is the frequency and Q_k the quality factor of the k^{th} longitudinal mode, which can be approximated by the ratio of Ω_k and the half-power bandwidth. Since the LIA provides RMS values, this point is at $2^{-0.5}(\approx 0.707)$ of the measured output voltage. V_R is the resonator volume, p_k is a mode dependent normalization coefficient and μ_k the reciprocal light-to-sound coupling factor of the k^{th} normal mode, respectively. $p_k(\vec{r})$ is the only factor depending on spatial coordinates. However, in case of first longitudinal mode excitation, which we exploit within our studies, the pressure only varies in z-direction and remains constant with respect to the tube radius r and angle θ. Thus, for the first longitudinal mode, the term $p_k(\vec{r})$ can be expressed as a sinusoidal half-wave ranging from 0 to 1

$$p_k(\vec{r}) \equiv p_1(z) = sin\left(z\frac{\pi}{L_R}\right) \tag{7}$$

Assuming an optimum light-to-sound coupling ($\mu_k \ll 1$) and considering the position of the microphone in the middle of the resonator ($\vec{r}\rightarrow\vec{r}_{\mathrm{mic}}$), i.e. $e^{-\mu_k}\cdot p_k(\vec{r})\rightarrow 1$, Eq. (6) simplifies to

$$p_a\left(\vec{r}_{\mathrm{mic}},\Omega_1\right) = \underbrace{(\gamma - 1)\frac{Q_1}{\Omega_1}\sqrt{2}\frac{L_R}{V_R}}_{\text{Cell constant } C_{\mathrm{cell}}}\alpha P_0 \tag{8}$$

with $p_k = \sqrt{2}$ in terms of the first longitudinal mode [24]. The ratio of resonator length and volume can obviously be considered constant if the node shifting phenomena is neglected and the PAC remains unmodified. Hence, the PA signal is directly proportional to the quality factor Q, the absorption coefficient α, the optical power P_0 and the decremented heat capacity ratio $(\gamma - 1)$, but indirectly proportional to the angular resonance frequency Ω, which is defined as $f_{\mathrm{res}} = \frac{\Omega}{2\pi}$.

3. Experimental

3.1. Laboratory setup

Fig. 1 illustrates a simplified block diagram of the gas stream of the laboratory test bench exhibiting three operation modes, namely (i) ***normal***, i.e. a dry gas mixture at atmospheric pressure, (ii) ***humidity*** and

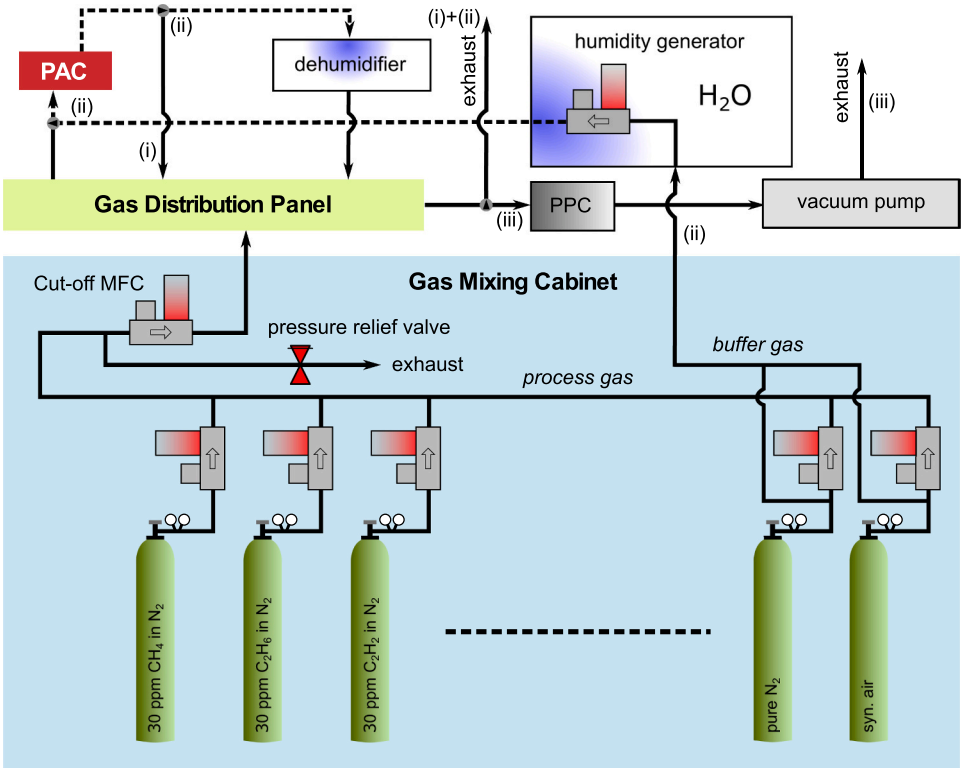

Fig. 1. Simplified block diagram of the gas stream of the laboratory test bench. Dashed lines indicate heated parts of the gas stream. Operation modes: (i) **normal**, (ii) **humidity**, (iii) **vacuum**.

(iii) ***vacuum*** mode. The gas mixture is set by means of mass flow controllers (MFC) (F-201CV-500-XXX) (Bronkhorst, Germany). After passing the Cut-off MFC, which sets the final flow rate between 20 and 500 ml/min, the gas mixture is led to the PAC. This setup allows to prepare various gas mixtures of high precision as well as to set a defined overall flow rate. To provide a defined humidification of the gas mixture, a humidity generator (HG) aGEPRO-V4 (ADROP Feuchtemeßtechnik GmbH, Germany) is connectible to the gas stream (operation mode (ii)). Since other gases may cause reactions within the HG, only N_2 or synthetic air can be led through the generator and mixed with other gases afterwards. After passing the PAC, the humidified gas is directed into a dehumidifier (TC-Standard 6111, Bühler Technologies GmbH, Germany). To prevent condensation inside the gas lines, HG and PAC as well as PAC and dehumidifier are coupled by temperature-controlled hoses (XtremeFLEX BS0052020 L, BriskHeat, US). In order to evaluate the PA signal's dependency on the pressure of the gas sample, a vacuum pump (Trivac D 2.5E, Leybold, Germany) and a pre-pressure controller (PPC) (P-702CV-6K0A-RAD-33-Z, Bronkhorst, Germany) were integrated into the test bench, referred to as operation mode (iii). Thus, the PPC can be set to any value between 1200 mbar and 200 mbar absolute pressure.

All test gases were provided by Westfalen AG (Germany). The purity of the dilution gases nitrogen (6.0) and synthetic air are specified by less than 0.1 ppmV of total hydrocarbon content. Each time the gas composition was changed, the gas stream system was flushed according to Weigl et al. [7]. All pre-diluted test-gases are specified by an analyte concentration of 30 ppmV and an accuracy of ± 3 %.

In this work, we used two interband cascade laser diodes emitting around 3365 nm and 3025 nm, which were manufactured and customized by nanoplus (Nanosystems and Technologies GmbH, Germany). The ICLs are mounted into a TO66 housing with integrated optics and temperature control, thus exhibiting an elliptic spot of radii 0.7 mm and 0.5 mm within the PAC. In terms of optical output power, we obtained 10.9 mW at 3368.8 nm (CH_4 excitation with an absorption cross-section σ_{CH4} = 4.9E-19 cm^2), 14.4 mW at 3363.0 nm (C_2H_6 excitation, σ_{C2H6} = 8.1E-19 cm^2) and 10.2 mW at 3025.8 nm (C_2H_2 excitation, σ_{C2H2} = 9.6E-19 cm^2) using a ThorLabs PM400 Power meter together with an S401C high-resolution thermal power sensor. The TO66 socket connects the respective ICL to an ILX Lightwave laser diode controller (LDC), model 3726 (Newport Corporation, US). The LDC is capable of separately controlling the laser current and the temperature of the ICL. The sine-modulated signal component required for WM-PAS is generated by a dual-channel function generator (FG) model 33522B (Keysight Technologies, US), which also provides an identical reference signal to the Lock-in amplifier (LIA) 7270 (Ametek, US). The frequency of modulation is set to half the resonance frequency of the acoustic resonator due to 2f – demodulation. The photoacoustic signal is monitored by means of an ultra-low noise MEMS microphone (ICS-40720, InvenSense Inc., US) which is read out in differential mode with a sensitivity according to the data sheet of – 32 dBV, i.e. 25.1 mV/Pa. A computer finally displays the photoacoustic amplitude as a plot of microphone signal over time. The individual electronic components are controlled by a LabVIEW (National Instruments, US) based in-house developed software. To ensure optimum operation parameters for the sine-modulated WM signal, offset-current, modulation depth and resonance frequency were determined by corresponding sweeps, i.e. reconstruction of the absorption peak by sweeping the DC component, a sweep of the modulation amplitude and a frequency sweep, respectively.

3.2. PAC design

Fig. 2 shows a cross-section view of the photoacoustic sensor including the gas flow indicated by dotted arrows. The sensor consisting of optics, PAC and temperature control circuit has overall dimensions of approx. 200×80×70 mm. A small opening in the middle of the resonator with 1 mm in diameter ensures a low-loss sound coupling to the microphone. The PAC with dimension of 90×40×40 mm is 3D metal printed using an aluminum alloy powder AlSi10Mg together with an M100 rapid prototyping machine (EOS GmbH, Germany) and is post-processed by conventional milling. In order to ensure a homogeneous temperature distribution within the resonator and the buffer volumes,

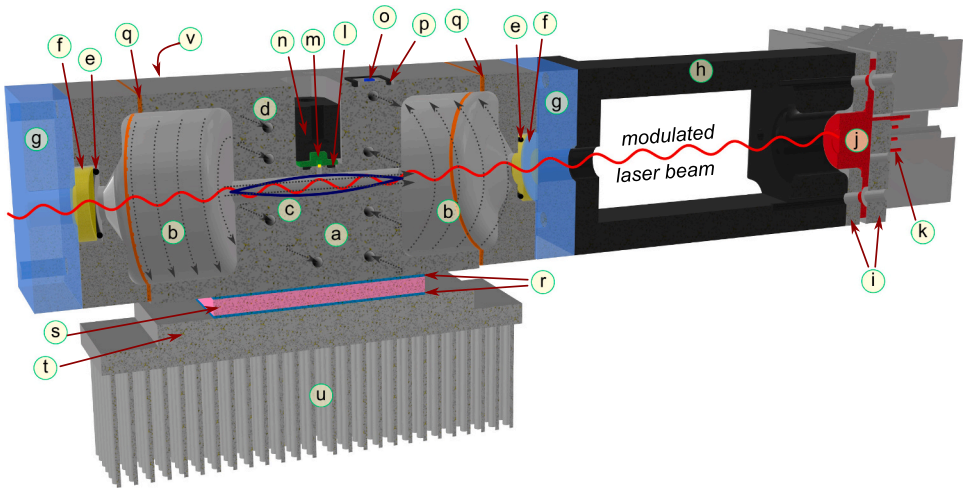

Fig. 2. Cross-section drawing of the sensor including a schematic visualization of the gas flow, laser beam and standing pressure wave ($L = \lambda/2$): **(a)** PAC, **(b)** buffer volume, **(c)** resonator, **(d)** helical gas flow, **(e)** radial seal (windows), **(f)** sapphire wedged window, **(g)** pressure plate, **(h)** spacer, **(i)** heat sink (ICL), **(j)** ICL in TO66 housing, **(k)** ICL connection pins, **(l)** radial seal (microphone), **(m)** MEMS microphone, **(n)** microphone holder, **(o)** *TpH*-sensor (including electronics are not depicted), **(p)** seal (*TpH*-sensor), **(q)** graphite seal (PAC), **(r)** thermal pad, **(s)** Peltier element, **(t)** aluminum plate, **(u)** heat sink (PAC), **(v)** NTC (back-mounted).

the PAC can be heated by means of a temperature control circuit with $PIDT_1$-behavior consisting of a TEC driver TEC-1089-SV (Meerstetter Engineering, Switzerland), an NTC B57861S0103F040 (TDK, Japan) and a Peltier element ET-161–12–08-E (European Thermodynamics LTD, UK) connected to an aluminum heat sink. This setup ensured a temperature stability of $\sigma = 0.01$ K. The NTC temperature sensor (v) for temperature feedback is fixed in a 10 mm blind hole on the backside of the PAC with thermal conductive glue. The MEMS microphone together with a corresponding screw-fixed 3D printed holder (m, n) are placed in a cut-out above the resonator center in order to provide a short out-coupling path of the acoustic signal. In terms of monitoring temperature *T*, pressure *p* and humidity *H* within the gas flow, a *TpH*-sensor BME280 (Robert Bosch GmbH, Germany) (o) is integrated on the top side of the PAC right before the gas output. Its data is pre-processed by integrated electronics on a printed circuit board (PCB) (not depicted in Fig. 2), which ensures communication via CAN interface. The gas sample is preheated by means of a helical channel, which is 3D-printed into the PAC. This prevents condensation of humidity on the inner cell walls on the one hand and assures a constant speed of sound on the other hand. Downstream of the preheating channel, the analyte gas enters the cylindrical buffer volume (b) tangentially assuring a laminar flow inside the resonator. The buffer volumes were designed and manufactured with rounded edges and smooth surfaces to avoid dead volumes or local turbulences. Their dimensions are 18.5 mm in length and 30 mm in diameter. The cylindrical resonator (c) is 4 mm in diameter and 31 mm in length, respectively, and was treated by a lapping rod and polishing paste (7 µm graining) in order to improve its surface quality.

The laser beam illuminates the PAC through wedged windows (f) WW30530-E1 (ThorLabs, US) to prevent optical cavities as well as back-reflections to the radiation source. Seals have been applied at several points in order to ensure gas tightness. For better thermal conductivity, the buffer volumes are attached via specially formed graphite seals (q). The laser diode (j) is actively cooled by an integrated Peltier element for excess heat dissipation in order to avoid thermally induced deterioration and assure constant emission of the laser diode. Hence, modular designed 3D metal printed heat sinks made of aluminum (i) have been used for ICL mounting. To prevent mutual interference between the temperature control circuits of PAC and ICL, a spacer (h) has been inserted between light source and PAC. This spacer ($l = 63$ mm) maintains a distance long enough to ensure a constant temperature and thus, a stable optical power of the ICL. The PAC is integrated into the laboratory gas stream by means of Swagelok screw connectors (Swagelok, US). A CAN-to-USB converter Zubax Babel (Zubax Robotics, Estonia) provides the data of the *TpH*-sensor to the computer. All sensitive cable connections are designed as coaxial cables with grounded shield to prevent possible signal interference.

4. Results and discussion

In this work, we present the performance of an ICL photoacoustic setup for the detection of low concentrations of methane, ethane and acetylene diluted in nitrogen and discuss the effects of ambient parameters such as temperature, pressure and mass flow on the photoacoustic signal. Furthermore, we investigated potential cross-sensitivities towards H_2O, O_2 as well as between the analytes among each other. Unless mentioned otherwise, the PAC temperature has been controlled at 40 °C, the mass flow has been set to 500 ml/min and the LIA roll off to 18 dB/octave, respectively. The acquired microphone signal is postprocessed as follows: (i) the microphone signal is demodulated and low pass filtered with a certain time constant τ_{LIA}, (ii) the resulting data is sampled with 5 Hz, (iii) the recorded data points are then averaged over a certain time. All measurements presented within this work are based on line-locked mode, i.e. no continuous wavelength scan mode was applied.

4.1. Calibration characteristics

The calibration characteristics are based on decremental analyte concentrations, i.e. prediluted analyte containing gas mixtures were further diluted in nitrogen, with every measuring point being averaged over 20 s. In accordance with theory (Eq. 8), the photoacoustic signal is directly proportional to the analyte concentration, thus yielding a linear calibration curve without offset, since there is basically no background signal in terms of WM-PAS. Table 1 lists some performance parameters of the sensor, namely sensitivity, noise level, LoD and the coefficient of linear fit determination. In terms of a better comparability to other optical systems, it also includes the normalized noise equivalent absorption coefficient (NNEA), which is calculated after

$$NNEA = \frac{LoD(3\sigma)\cdot N_A\cdot\sigma\left(\tilde{\nu}_{Ph}\right)\cdot P_{opt}}{\mathrm{SNR}\cdot\sqrt{\Delta f\cdot V_{mol}}} = \frac{LoD(3\sigma)\cdot\alpha_N(\lambda_{Ph})\cdot P_{opt}}{\mathrm{SNR}\cdot\sqrt{\Delta f\cdot N}} \quad (9)$$

where $\alpha_N(\lambda_{Ph})$ is the absorption coefficient, *N* is the volume ratio of the analyte and Δf is the equivalent noise bandwidth (ENBW) of the LIA. The SNR is 3 since we use three times the standard deviation for calculating the LoD. An Allan deviation of the PAC setup revealed white noise to dominate and yielded a potential 50 % LoD improvement by increasing the averaging time to 100 s. Individual calibration curves together with corresponding Allan deviation plots are depicted in the appendix (see Figs. 11–13).

Table 1
Summary of the different calibration characteristics. The LIA time constant was set to τ_{LIA} = 2 s in terms of methane and acetylene and to τ_{LIA} = 5 s regarding ethane detection, the averaging time was set to 20 s.

Analyte gas	Sensitivity [μV/ppmV]	R^2	LoD (3σ) [ppbV]	Noise level (3σ) [nV]	NNEA [W cm^{-1}Hz$^{-0.5}$]
Methane	2.62	0.9999	6.8	17.8	$1.6 \cdot 10^{-9}$
Ethane	8.55	1.0000	2.3	19.6	$1.8 \cdot 10^{-9}$
Acetylene	5.74	1.0000	3.6	20.8	$1.5 \cdot 10^{-9}$

4.2. Influence of environmental parameters

4.2.1. Influence of temperature

The influence of the gas temperature on the photoacoustic signal was investigated while heating the PAC from 20 °C to 50 °C with steps of 5 K. After the set temperature stabilized, an incremental frequency sweep was performed, while every measurement was recorded with τ_{LIA} = 2 s and averaged over 60 s. The respective resonance profiles with acetylene as an analyte are depicted in Fig. 3. The results demonstrate that temperature changes affect the photoacoustic signal similar to Weigl et al. [7].

By heating the PAC from 20 °C to 50 °C, we observed the photoacoustic magnitude to linearly decrease (R^2 = 0.9997) by 19.5 %. This drop can be assigned to three different phenomena as follows. In line with this overall signal drop, the heating was empirically identified to cause the resonance frequency to increase by 4.4 %, i.e. 7.3 Hz/K, as well as the Q factor to decrease by 3.4 %. In addition, the absorption coefficient was calculated via HITRAN-based simulation to decrease by 12.3 %. Including these individual loss terms with respect to their proportionality according to Eq. (8) results in a total theoretical signal drop of 18.9 %, which is in good agreement with the overall experienced signal drop of 19.5 %.

While the increase in resonance frequency obviously results from an accelerated speed of sound, the Q factor has already been identified to decrease with increasing temperature in former studies [11,12] due to augmented energy dissipation caused by enhanced molecular movement. Measurements regarding methane exhibit an analog behavior (see appendix, Fig. 14).

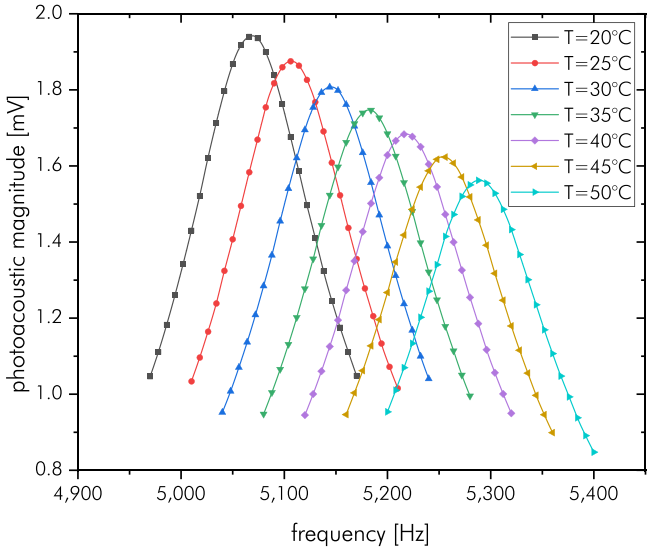

Fig. 3. Temperature dependency of resonance profiles. The gas mixture contained 300 ppmV acetylene diluted in nitrogen. The measuring points are connected by Akima-Interpolation.

4.2.2. Influence of pressure

To evaluate the photoacoustic signal's dependency on the pressure of the gas sample, the data was acquired on the lines of the analysis depicted in Fig. 3, i.e. by means of frequency sweeps, with only τ_{LIA} being extended to 5 s. Initially, we carried out a long-term experiment without mass flow at approx. 10 mbar which proved the tightness of the PAC. After that, two series of measurements were performed based on mixtures of 15 ppmV C_2H_2 and CH_4 diluted in N_2, respectively, while the pressure was varied between 1000 mbar and 300 mbar.

Fig. 4a indicates the photoacoustic signal to drop non-linearly with decreasing pressure, i.e. signal attenuation gains influence at low pressure. While a linear signal drop would have been expected due to diminution of the overall molecular density, hence lowering the number of light absorbing analyte molecules, non-linearity seems surprising at first. However, further investigations (see Fig. 4b) revealed a similar dependency of the resonance frequency on the pressure. Considering that the speed of sound does not depend on the overall pressure, i.e. the length of the standing acoustic wave solely depends on the length of the resonator tube, the pressure within the PAC is not expected to affect its resonance frequency at all. Therefore, we assume the well-known effect of node shifting [27,28] to be responsible and to gain influence when reducing the particle density, yielding an increased red-shift of the frequency.

Fig. 5 combines the information of Fig. 4a and b by plotting the

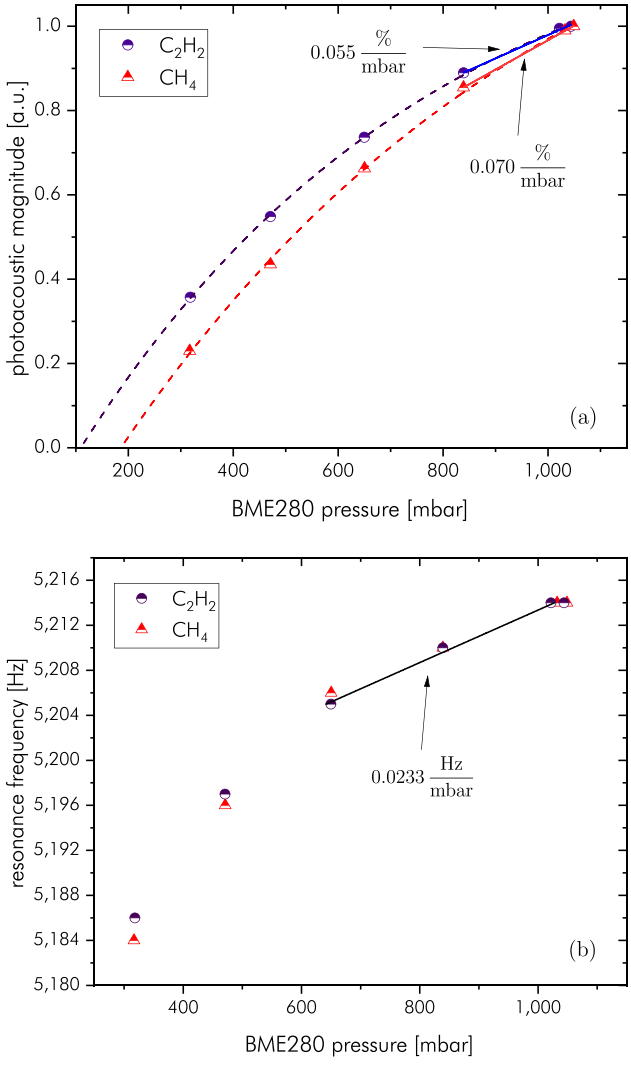

Fig. 4. Influence of pressure on the photoacoustic signal (a) and resonance frequency (b).

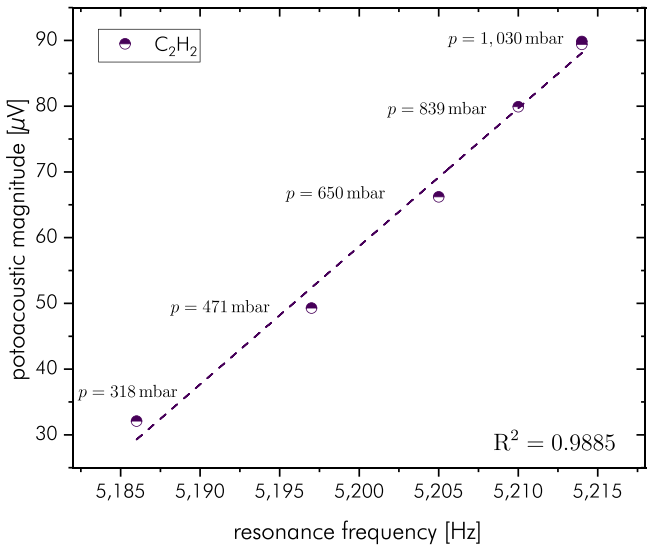

Fig. 5. Relationship between photoacoustic signal and resonance frequency applying a partial vacuum. The gas mixture contained 15 ppmV acetylene diluted in nitrogen.

photoacoustic signal against the resonance frequency of the system using the example of C_2H_2 in N_2, ignoring that the data was gathered at different total pressures.

Fig. 5 indicates direct proportionality between the photoacoustic magnitude and the resonance frequency, whereas theory predicts a reciprocal dependency. We interpret this contrary by counteracting of the frequency dependency on the pressure (see Fig. 4b) and the signal dependency on the frequency (see Eq. 8), respectively, which can be considered invers. This yields a compensation of non-linearities and finally a linear signal dependency on the frequency (see Fig. 5), once changes in resonance frequency are caused by pressure variations. In terms of methane, we obtained analogous results (see appendix, Fig. 15).

Concluding this section, there are various effects how the pressure of the gas sample influences the photoacoustic signal. Aside from those already discussed, i.e. changing analyte particle density and shifting of the resonance frequency, complex mechanisms cause pressure variations also to affect loss-terms resulting in quality factor variation or collision broadening yielding absorption cross-section variation. Nonetheless, we found those effects either to affect the PA signal linearly or to be negligible compared to the phenomenon of node shifting. Moreover, in view of developing a sensor for standard ambient conditions, the observed signal drop due to pressure decrease can be considered linear in the atmospheric range between about 1030 mbar and 850 mbar, thus allowing easy calibration.

4.2.3. *Influence of mass flow*

To ensure a gas-tight PAC, the mass flow was varied in a range from 50 ml/min to 500 ml/min, while all other parameters remained unmodified. The results show a linearly decreasing flow ($R^2 = 0.9999$) with 0.52 % signal deterioration per 100 ml/min mass flow delta. However, we identified this dependency to result from a mass flow induced pressure change of several mbar inside the PAC applying operation mode (i). As the ratio of pressure and photoacoustic signal can be regarded as constant within the range of applied mass flow, no direct physical correlation of the PA signal with flow rate was observed. The effect of indirect pressure induced correlation can be corrected easily by monitoring the pressure inside the PAC.

4.3. *Influence of cross-sensitivities*

The impact of ambient air molecules, i.e. H_2O and O_2, on the photoacoustic signal (amplitude and phase) in terms of monitoring CH_4 and C_2H_2 diluted in N_2 as well as mutual interactions of the analyte molecules were investigated in detail. With regard to the measurements dealing with humidified gas, the laboratory test bench was configured to operation mode (ii) including the HG (refer to Fig. 1). On the lines of ambient parameter analysis, the data was acquired by means of frequency sweeps in order to ensure optimum resonance amplification. The flow rate uncertainty increases when applying operation mode (ii), thus it is accompanied by distinct signal fluctuations. Therefore τ_{LIA} was set to 10 s once humidification was used.

Table 2
Processes including rate constants involved to the de-excitation of methane upon self-collisions or via collisions with oxygen, water and nitrogen, respectively. Reactions labeled in **bold** correspond to VT-processes, the others to VV-processes. Regarding superscript "a", Barreiro et al. assumed typical values. Superscript "b" indicates a manual rate adjustment within the error specifications stated in literature.

	Reaction	Reaction rate k in [Hz atm^{-1}]
(1)	$CH_4(\nu_{s1}) + M \xrightarrow{k_1^M} CH_4(2\nu_b) + M$	$k_1^{CH_4} = 2.1{\cdot}10^8$ [34] $k_1^{N_2} = 4.6{\cdot}10^8$ [35] $k_1^{H_2O} = 1{\cdot}10^8$ [36]a $k_1^{O_2} = 4.6{\cdot}10^8$ [35]
(2)	$CH_4(2\nu_b) + CH_4 \xrightarrow{k_2} CH_4(\nu_b) + CH_4(\nu_b)$	$k_2 = 2{\cdot}2.4{\cdot}10^8$ [37]; $2{\cdot}2.5{\cdot}10^8$ b
(3)	$CH_4(2\nu_b) + H_2O \xrightarrow{k_3} CH_4(\nu_b) + H_2O(\nu_2)$	$k_3 = 2{\cdot}2{\cdot}10^7$ [36]a; $2{\cdot}8{\cdot}10^7$ b
(4)	$CH_4(2\nu_b) + O_2 \xrightarrow{k_4} CH_4(\nu_b) + O_2(\nu)$	$k_4 = 2{\cdot}3.3{\cdot}10^6$ [37]; $2{\cdot}4{\cdot}10^6$ b
(5)	$CH_4(2\nu_b) + M \xrightarrow{k_5^M} CH_4(\nu_b) + M + \Delta E$	$k_5^{CH_4} = 2{\cdot}7.9{\cdot}10^5$ [37] $k_5^{N_2} = 2{\cdot}(8 \pm 1){\cdot}10^4$ [33]; $2{\cdot}7{\cdot}10^4$ b $k_5^{H_2O} = 2{\cdot}10^5$ [36]a $k_5^{O_2} = 2{\cdot}1.3{\cdot}10^5$ [33]
(6)	$CH_4(\nu_b) + H_2O \xrightarrow{k_6} CH_4 + H_2O(\nu_2)$	$k_6 = 2{\cdot}10^7$ [36]a; $8{\cdot}10^7$ b
(7)	$CH_4(\nu_b) + O_2 \xrightarrow{k_7} CH_4 + O_2(\nu)$	$k_7 = 3.3{\cdot}10^6$ [37]; $3.3{\cdot}10^6$ b
(8)	$O_2(\nu) + H_2O \xrightarrow{k_8} O_2 + H_2O(\nu_2)$	$k_8 = 3.7{\cdot}10^7$ [38]; $3.5{\cdot}10^7$ b
(9)	$O_2(\nu) + CH_4 \xrightarrow{k_9} O_2 + CH_4(\nu_b)$	$k_9 = 3.27{\cdot}10^7$ [37]
(10)	$H_2O(\nu_2) + CH_4 \xrightarrow{k_{10}} H_2O + CH_4(\nu_b)$	$k_{10} = 2{\cdot}10^7$ [36]a
(11)	$CH_4(\nu_b) + M \xrightarrow{k_{11}^M} CH_4 + M + \Delta E$	$k_{11}^{CH_4} = 7.9{\cdot}10^5$ [37] $k_{11}^{N_2} = (8 \pm 1){\cdot}10^4$ [33]; $7{\cdot}10^4$ b $k_{11}^{H_2O} = 1.2{\cdot}10^5$ [36]a $k_{11}^{O_2} = 1.3{\cdot}10^5$ [33]
(12)	$O_2(\nu) + M \xrightarrow{k_{12}^M} O_2 + M + \Delta E$	$k_{12}^{CH_4} = 6{\cdot}10^5$ [39] $k_{12}^{N_2} = 40$ [40] $k_{12}^{H_2O} = 1.1{\cdot}10^6$ [40] $k_{12}^{O_2} = 66$ [41]
(13)	$H_2O(\nu_2) + M \xrightarrow{k_{13}^M} H_2O + M + \Delta E$	$k_{13}^{CH_4} = 1{\cdot}10^6$ [36]a; $1.2{\cdot}10^6$ b $k_{13}^{N_2} = 1{\cdot}10^6$ [38] $k_{13}^{H_2O} = 1.2{\cdot}10^9$ [41] $k_{13}^{O_2} = 1{\cdot}10^6$ [38]

4.3.1. *Kinetic modeling of molecular relaxation processes*

During our investigations regarding the influence of water and oxygen on the photoacoustic signal of methane (see 4.3.2, 4.3.3 and 4.3.4, respectively), we identified changes in signal amplitude, accompanied by a phase lag ϕ, which is defined by

$$\phi = arctan(\omega\tau_n) \tag{10}$$

with τ_n being the time which is needed for non-radiative relaxation.

Therefore, we assume a varying amplitude together with a changing phase lag mainly to be due to changes within the path of molecular relaxation, induced by the presence of water and/or oxygen. In order to confirm that this theory of molecular relaxation is responsible for PA signal variation due to changes in the bulk composition, we performed a MATLAB based simulation in order to calculate the theoretical photoacoustic magnitude and phase. Therefore, we considered the parameters CH_4 volume ratio, optical power, excitation wavenumber, resonance frequency, volume density as well as all relevant molecular relaxation paths (see Table 2). For simplification reasons, the individual vibrational modes of CH_4 were combined into two clusters, named polyads [29]. The energetically lower one (dyad ν_b) includes the ν_2 and ν_4 bending modes in the 1100 – 1500 cm^{-1} region [30]. The upper cluster (pentad) consists of five vibrational modes, i.e. the ν_1 and ν_3 stretching modes located at approx. 3000 cm^{-1} as well as the harmonics of the bending modes $2\nu_2$, $2\nu_4$ and $\nu_4 + \nu_2$. In fact, according to [31] we subdivided the pentad into the two groups ν_{s1} and $2\nu_b$, in terms of simulation, with ν_{s1} merging the stretching modes and $2\nu_b$ the harmonics of the bending modes, respectively. To gain a better understanding, Fig. 6 depicts the energy levels we considered regarding relaxation. According to Hunter et al. [32], F is the initial number of quanta absorbed per second per unit volume ($s^{-1}m^{-3}$):

$$F = \rho_{CH4} \cdot \sigma\left(\tilde{\nu}_{Ph}\right) \cdot \Psi_0 \tag{11}$$

We classify three types of molecular collisions, i.e. VT when the total vibrational energy is released as heat into the system, VV when some of the vibrational energy is transferred to vibrational energy of the collision partner and collisions entailing no energy transition at all, respectively. However, a VV energy transfer caused by inelastic collision is more likely to occur if the involved vibrational states are of similar energy, e.g. $CH_4(2\nu_b) \approx CH_4(\nu_b) + O_2(\nu)$. In terms of our simulations we considered all transitions illustrated in Fig. 6 by adopting the corresponding relaxation rates from literature (see Table 2). The illustrated transitions involve 28 relaxation processes. In some cases we introduced minor changes to the relaxation rates, but these were well within the error specifications of the literature values stated in Table 2. Our calculations are based on the kinetic relaxation model of [32]. Accordingly, the heat production rate $\dot{H}(t)$, that is responsible for photoacoustic signal generation, represents the sum of every single heat released from n involved vibrational states

$$\dot{H}(t) = \sum_{i=1}^{n} \dot{H}_i(t) \tag{12}$$

The individual heat components $\dot{H}_i(t)$ can be calculated by multiplying the respective vibrational energy $h\nu_i$ with the population density of the excited state $[\nu_i]$, which is a complex function, and the sum of m reaction rates k_j from the i-state to the j-state [32]:

$$\dot{H}_i(t) = [\nu_i] \cdot \left(\sum_{j=1}^{m} k_j \cdot h\Delta\upsilon_{i\to j} \right) \tag{13}$$

The total heat production rate from Equation (12) can be directly linked to a photoacoustic pressure [31]. In order to obtain the complex photoacoustic signal U_{PA} in electric voltage unit [V], the cell constant C_{cell} and the microphone sensitivity S finally have to be considered as well.

$$U_{PA} = S \cdot C_{cell} \cdot \alpha P_0 = \underbrace{S \cdot C_{cell} \cdot \pi r_{beam}^2}_{C_{sim}} \cdot \dot{H}(t) \tag{14}$$

The empirical factor C_{sim} was used to convert the calculated heat production rate $\dot{H}(t)$ into the complex photoacoustic signal U_{PA}. Regarding the restricted scope of this work and for clarity reasons, a subsequent publication providing a detailed description of the kinetic model is intended.

4.3.2. *Impact of H_2O on CH_4 diluted in N_2*

This section deals with the humidification of a gas sample containing 15 ppmV methane diluted in nitrogen, while N_2 was also used as carrier gas for the HG. The results of the measurement are presented in Fig. 7, where 2-y-axis plotting is used to show both, photoacoustic amplitude and phase. While the red triangles and the orange circles represent the empirically determined amplitude and phase values, the red solid line and the orange dashed line visualize the simulated data, respectively. Most obviously, the photoacoustic amplitude is significantly lower when

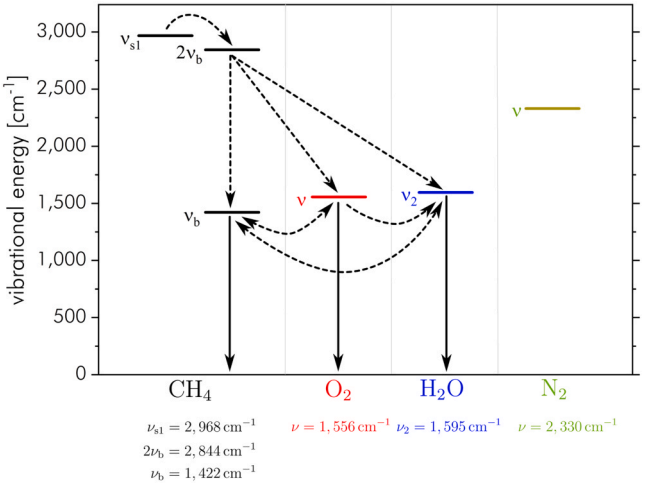

Fig. 6. Vibrational states of CH_4, O_2, H_2O and N_2. Possible VV-transitions are indicated as dashed arrows, solid arrows represent VT-transitions.

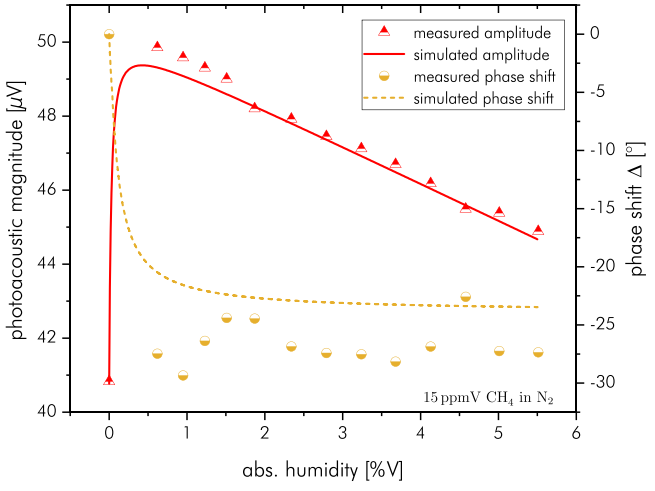

Fig. 7. Measured amplitude (red triangles) and phase (orange circles) as well as simulated amplitude (red solid line) and phase shift (orange dashed line) with rising H_2O concentration for 15 ppmV CH_4 diluted in N_2.

no water is present, though adding 0.6 %V-H_2O already causes the amplitude to increase by 22 %. Our simulations revealed that this is due to the fact that not all vibrational states excited at 2968.4 cm^{-1} are able to relax completely during one period of modulation in the absence of water, but relaxation is accelerated by humidification. However, this rise in amplitude is not only attributed to faster VT-relaxation of CH_4, but also to a fast VV-transition from $CH_4(\nu_b)$ to $H_2O(\nu_2)$ with subsequent VT-relaxation of water (Table 2, transitions 11, 6 and 13).

With rising humidity, the measured signal amplitude decreased linearly ($R^2 = 0.9925$) by 1.4 µV/%V-H_2O. Since the phase lag remained rather constant, we exclude relaxation effects to be responsible for this decrease in amplitude. This assumption is substantiated by the fact, that the phenomenon of a decreasing amplitude by further humidification appears in all measurements to be approx. 2 %/%V-H_2O (see Figs. 7, 9 and 10). Although we determined the decremented heat capacity ratio as well as the ratio of quality factor and resonance frequency to decrease linearly, the empirical observed amplitude deterioration exceeds the theoretical calculation according to Eq. (8). Therefore, we cannot ultimately assign a clear reason for this phenomenon so far but assume an artifact of our measurement setup to be accountable, too. By implementing this analyte independent amplitude deterioration into our calculation, we obtained the simulated photoacoustic amplitude with an accuracy of at least 98 %, which is in good agreement with the empirical data. Besides photoacoustic signal interference, water was identified to cause the resonance frequency to blue-shift by approximately 7.4 Hz/% V-H_2O, which is in line with the theory of speed of sound.

4.3.3. Impact of O_2 on CH_4 diluted in N_2

Within this section, we discuss the influence of oxygen on the photoacoustic signal originating from 15 ppmV CH_4 diluted in N_2. A strong decrease in magnitude (79.7 %) and a phase shift (19.5°) were observed by adding 8.2 %V-O_2, respectively. While the frequency drop of 3.8 Hz/%V-O_2 is in line with the theory of speed of sound, the distinct decrease in amplitude was identified to result from delayed relaxation, i.e. a very fast VV energy transfer from $CH_4(\nu_b)$ to $O_2(\nu)$ (Table 2, transition 7). Due to very slow subsequent VT-relaxation of O_2 (Table 2, transition 12), a significant quantity of the internal energy cannot be released as kinetic energy into the system at the given measuring conditions. As a result, the major part of the energy of the initially excited CH_4 streching mode at 2968 cm^{-1} finally accumulates in the O_2 vibrational state at 1556 cm^{-1} [33]. This energy transfer from methane to oxygen yielding pronounced PA amplitude deterioration is in accordance with the findings of Barreiro et al. [31]. On the lines of Fig. 7, Fig. 8 visualizes the empirical and simulated data, respectively, thus proving the kinetic model that forms the basis for our interpretation.

4.3.4. Impact of O_2 and H_2O on CH_4 diluted in N_2

While the previous section dealt with the successive addition of oxygen to a CH_4 in N_2 mixture, thus affecting the PA signal due to delayed relaxation, this section is meant to further investigate the impact of H_2O. For this reason, water was successively added to a mixture containing a constant methane volume ratio of 15 ppmV diluted in 90 %V-N_2 and 10 %V-O_2. Fig. 9 indicates that the signal drop caused by O_2 is completely compensated by the addition of even small amounts of H_2O, i.e. the acceleration of relaxation causes the amplitude to increase by a factor of 6.6. Due to extended complexity of the composition and with another view to Table 2, we expect complex VV-transfers to take place. Nonetheless, besides general VT-acceleration by H_2O, two VV-reactions can be highlighted in order to understand how water promotes the relaxation of the system. On the one hand the VV-transition from $CH_4(\nu_b)$ to $H_2O(\nu_2)$ (Table 2, transition 6) competes with the VV energy transfer from $CH_4(\nu_b)$ to $O_2(\nu)$, while on the other hand energy that is already accumulated in $O_2(\nu)$ in turn can be retrieved according to reaction (8) in Table 2. Finally, both reactions result in the excitation of H_2O bending vibrations followed by subsequent fast VT-relaxation (Table 2, transition 13). The successive signal deterioration with rising humidity by approx. 2 %/%V-H_2O is almost identical to the measurements in pure nitrogen (see Fig. 7).

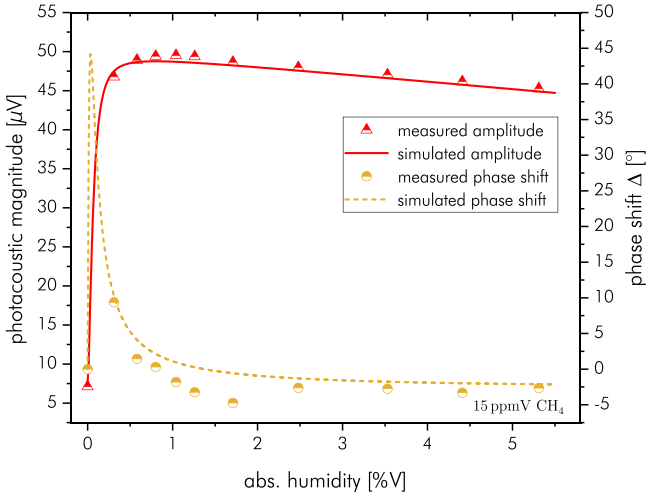

Fig. 9. Measured (points) and simulated (solid lines) amplitude and phase shift with rising H_2O concentration for 15 ppmV CH_4 diluted in N_2 and O_2.

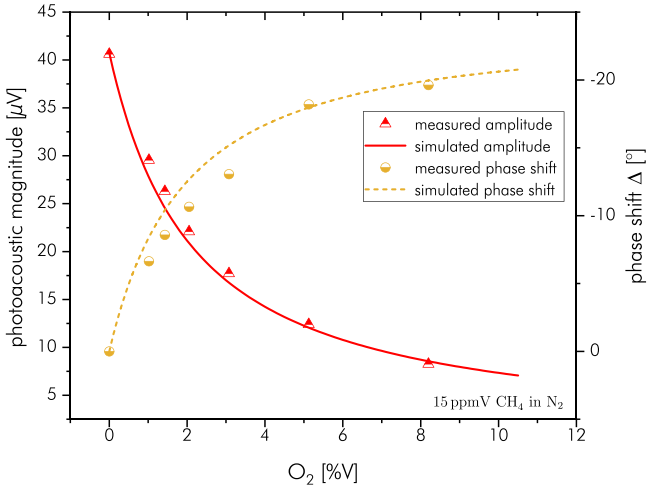

Fig. 8. Measured (points) and simulated (solid lines) amplitude and phase shift with rising O_2 concentration for 15 ppmV CH_4 diluted in N_2. The phase ordinate is plotted reversed.

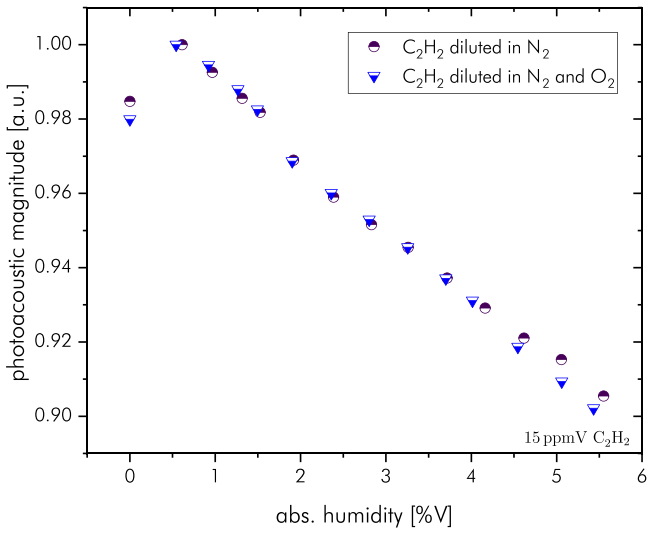

Fig. 10. Photoacoustic amplitude of 15 ppmV C_2H_2 diluted in N_2 together with a rising H_2O concentration in N_2 (blue triangles) and N_2 and O_2 (dark-blue circles), respectively.

4.3.5. *Impact of H_2O and O_2 on C_2H_2 diluted in N_2*

Besides methane, we investigated cross-sensitivities that might affect photoacoustic acetylene detection. On the lines of Sections 4.3.2 and 4.3.4, we used a mixture with a constant volume ratio of 15 ppmV acetylene diluted in N_2 and 90 %-N_2 + 10%-O_2, respectively, and successively added H_2O (see Fig. 10). As no change in photoacoustic phase was observed, only the respective amplitudes are plotted. Comparing both measurements with the corresponding methane measurements (refer to Figs. 7 and 9), the rise of the amplitude by addition of small amounts of water is far less pronounced in case of C_2H_2. Along with the finding of a constant photoacoustic phase, we therefore assume that the addition of H_2O is not affecting the relaxation path of these gas compositions. Due to a lack of rate constants in literature, no kinetic modeling was carried out so far in terms of acetylene by our group. We rather assume this slight increase in PA magnitude by adding small amounts of H_2O to acetylene containing mixtures to result from a change in mass flow with added HG instead. With a decrease in photoacoustic amplitude which is analogous to previous measurements (see Figs. 7 and 9) by approx. 2 %/%V-H_2O in pure nitrogen as well as in a mixture of 90 %-N_2 / 10 %-O_2, respectively, the findings are in accordance with those containing methane as analyte species, thus supporting our theory of an analyte independent signal deterioration (refer to Section 4.3.2). The resonance frequency was observed to shift linearly by approx. 7.3 Hz/% V-H_2O coinciding with the theory of speed of sound. Since adding water to acetylene mixtures has almost the same effect, regardless of the employed dilution gas, and no change in photoacoustic phase was observed, we assume complete molecular relaxation.

4.3.6. *Mutual interactions of analyte species*

As a final cross-sensitivity experiment, we investigated mutual interactions of the analytes methane, ethane and acetylene. More precisely, we examined the influence of acetylene and ethane on methane detection as well as the influence of methane on acetylene detection. Since all test gases were diluted in nitrogen and the gas temperature was maintained constant, no change in the speed of sound was to be expected, forgoing the need of adjusting the modulation frequency.

In a first step, 10 ppmV ethane was successively added to a mixture containing 15 ppmV CH_4, yielding a considerable cross-sensitivity causing a linear ($R^2 = 0.9973$) amplitude loss of approx. 0.9 %/ppmV-C_2H_6 (see appendix, Fig. 16). This loss can be attributed to deformation of the CH_4 peak. Although the ethane peak (3363 nm) is 5.8 nm next to methane absorption, there is still spectral interference at the methane region at 3368 nm with an absorption cross-section of σ= 1.6E-19 cm^2 according to HITRAN data. However, this effect mitigates with rising CH_4 concentration since the relative impact on peak deformation is obviously less pronounced in case of strong CH_4 absorption. One conclusion that can be drawn regarding this effect reads as follows: In applications with fluctuating ethane concentration, measurements should be performed at partial vacuum and reduced modulation index, respectively. Although, this results in a poorer sensitivity and detection limit, reduced pressure yields separation of the absorption peaks of methane and ethane, thus counteracting the influence of cross-sensitivities.

In contrast, no discernible influence of methane on photoacoustic acetylene detection was identified and vice versa.

5. Conclusion

We developed a highly sensitive photoacoustic system for detecting the three hydrocarbons methane, ethane and acetylene, while the detection of methane and ethane was accomplished by one single ICL. With 3σ detection limits of 6.8 ppbV, 2.3 ppbV and 3.6 ppbV, respectively, we provide a solid basis for trace gas analysis of these analytes diluted in nitrogen. Besides, we investigated the influences of ambient parameters like gas temperature, pressure and mass flow, cross-sensitivities towards H_2O and O_2 as well as mutual interactions of the analyte species.

The influence of gas temperature was studied by heating the gas sample from 20 °C to 50 °C in terms of acetylene detection. Thus, we found the resonance frequency to blue-shift according to the theory of speed of sound as well as the PA amplitude to decrease by 19.5 %. By decreasing order, the sources of signal attenuation were conclusively identified, namely less absorption, resonance frequency shifting and quality factor deterioration. The dependency of resonance frequency and PA magnitude on the pressure of the gas sample was found to be more complex, both revealing non-linear correlations. However, non-linearity was determined to exclusively result from the fact, that node shifting gains influence at low pressures. Moreover, the presented results demonstrate that the flow rate does not directly affect the photoacoustic signal, but causes a change in pressure, which in turn yields a change in the PA amplitude.

With regard to cross-sensitivity evaluation, we investigated the dependency of trace gas concentrations of acetylene and methane diluted in nitrogen on changing O_2 and H_2O concentrations, respectively. Every series of measurements where water was added to the composition revealed a continuous decline in amplitude without affecting the phase of the photoacoustic signal. Therefore, we excluded relaxation effects to be responsible and rather assume an artifact of our measurement setup to affect amplitude deterioration by humidification, too. While in terms of acetylene no further mentionable cross-sensitivities towards O_2 or H_2O were observed, photoacoustic methane detection was found to suffer from various interferences.

A kinetic model was used in order to simulate the relaxation path of photoacoustic signal generation. The model considers the composition of the gas mixture, the optical power, all relevant vibrational states (refer to Fig. 6), the resonance frequency, the volume density as well as all relevant molecular relaxation paths (see Table 2). By means of this model we were able to assign those various interferences to molecular relaxation phenomena. As for restricted extent of this work and for clarity reasons, a publication providing a detailed description of the model is intended.

Concluding, methane detection was identified to suffer from cross-sensitivities towards ethane as well, due to alteration of its absorption peak shape. However, acetylene was determined not to affect methane detection or vice versa.

Our comprehensive investigations regarding environmental and cross-sensitivity analysis provide a better understanding of photoacoustic systems in general and relaxation related effects in particular. Knowing and understanding these effects allows for maintaining detection limits in the sub-ppmV-range even in real life conditions, i.e.

changes of environmental parameter or in composition. Therefore, our compact photoacoustic sensor has great potentials for cross-sensitivity resilient trace gas analysis.

Funding

Essential financial support for this work has been provided within the scope of the projects µPASII and PreSEDA funded by the German government and the Federal Ministry of Economic Affairs and Energy (BMWi). The funding codes of these projects are 03ET1317A and 03EN2028A.

CRediT authorship contribution statement

Jonas Pangerl: Conceptualization, Data curation, Funding acquisition, Investigation, Methodology, Project administration, Visualization, Writing original draft, Writing – review & editing, Max Müller: Conceptualization, Data curation, Investigation, Methodology, Software, Visualization, Writing – review & editing, Stefan Weigl: Conceptualization, Software, Writing – review & editing, Thomas Rück: Conceptualization, Methodology, Supervision, Validation, Writing – review & editing, Funding acquisition, Rudolf Bierl: Funding acquisition, Project administration, Supervision, Validation, Writing – review & editing.

Declaration of Competing Interest

The authors declare that they have no known competing financial interests or personal relationships that could have appeared to influence the work reported in this paper.

Appendix

See Figs. 11–16.

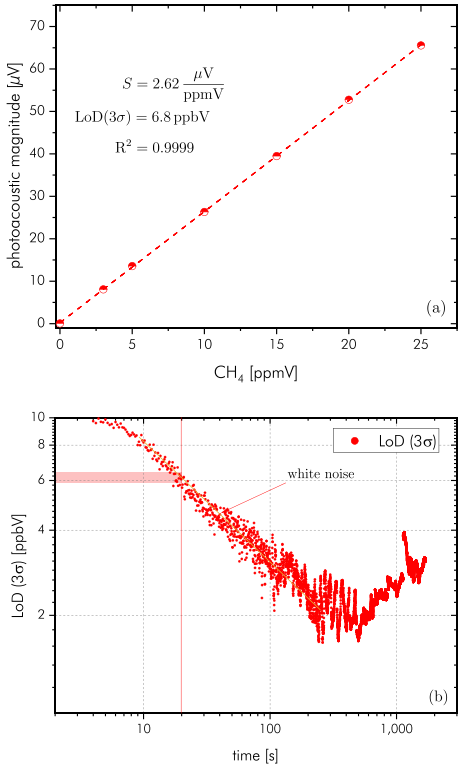

Fig. 11. Calibration curve (a) and Allan deviation plot (b) of methane in pure nitrogen. Since the same light source is used in terms of ethane detection, the Allan deviation measurement points are identical to Fig. 12b.

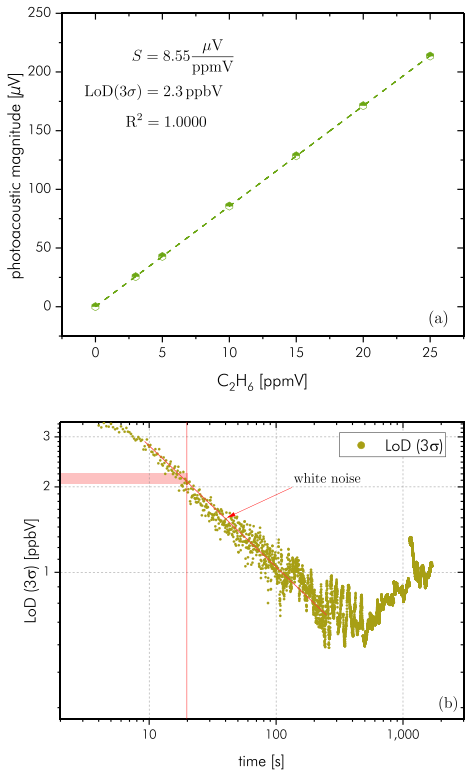

Fig. 12. Calibration curve (a) and Allan deviation plot (b) of ethane in pure nitrogen.

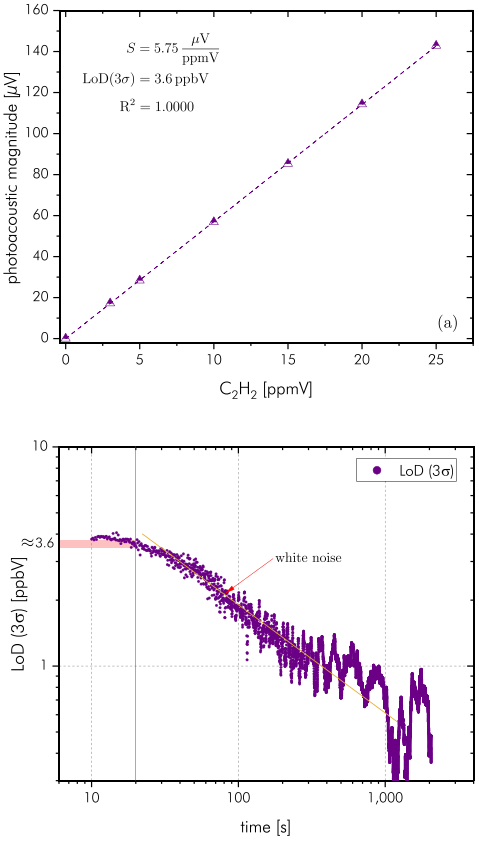

Fig. 13. Calibration curve (a) and Allan deviation plot (b) of acetylene in pure nitrogen.

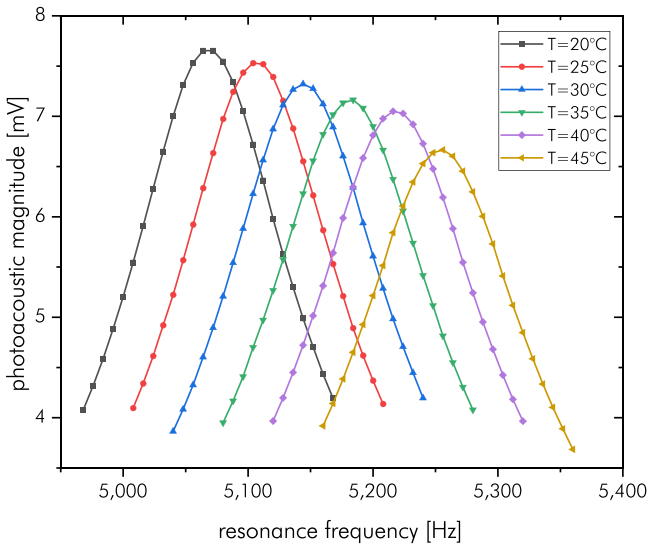

Fig. 14. Temperature dependency of resonance profiles. Tha gas mixture contained 2500 ppmV methane diluted in nitrogen. The measuring points are connected by Akima-Interpolation.

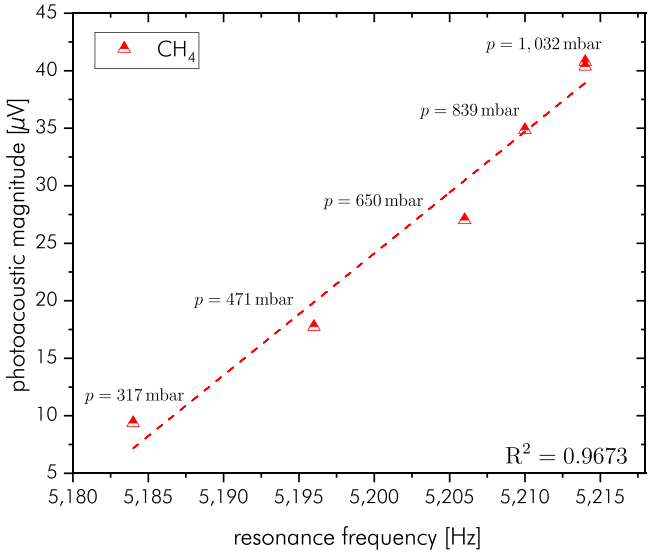

Fig. 15. Relationship between photoacoustic signal and resonance frequency applying a partial vacuum in terms 15 ppmV methane diluted in nitrogen.

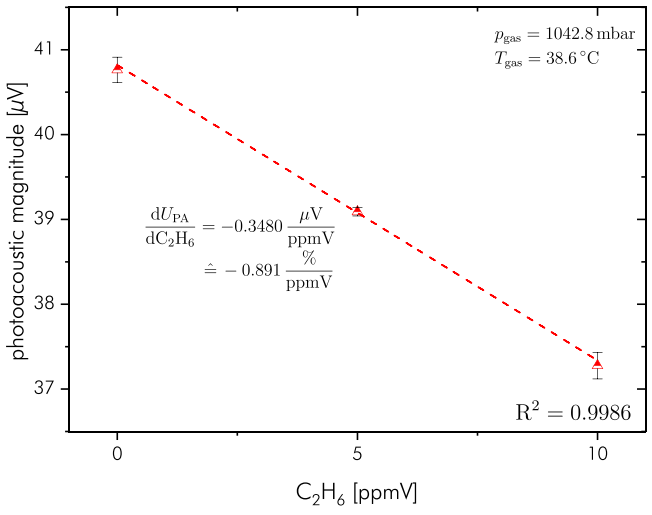

Fig. 16. Influence of ethane to the photoacoustic signal of 15 ppmV methane diluted in nitrogen.

References

[1] T.M. Coelho, E.C. Vidotti, M.C. Rollemberg, A.N. Medina, M.L. Baesso, N. Cella, A. C. Bento, Photoacoustic spectroscopy as a tool for determination of food dyes: comparison with first derivative spectrophotometry, Talanta 81 (1–2) (2010) 202–207.

[2] J. Irudayaraj, H. Yang, S. Sakhamuri, Differentiation and detection of microorganisms using fourier transform infrared photoacoustic spectroscopy, J. Mol. Struct. 606 (1–3) (2002) 181–188.

[3] C. Popa, Ethylene measurements from sweet fruits flowers using photoacoustic spectroscopy, Molecules 24 (6) (2019) 1144.

[4] M.J. Navas, A.M. Jiménez, A.G. Asuero, Human biomarkers in breath by photoacoustic spectroscopy, Clin. Chim. Acta 413 (15–16) (2012) 1171–1178.

[5] D.C. Dumitras, M. Petrus, A.-M. Bratu, C. Popa, Applications of near infrared photoacoustic spectroscopy for analysis of human respiration: a review, Molecules 25 (7) (2020) 1728.

[6] S. Weigl, F. Feldmeier, R. Bierl, F.-M. Matysik, Photoacoustic detection of acetone in N2 and synthetic air using a high power UV LED, Sens. Actuators B Chem. 316 (2020), 128109.

[7] S. Weigl, E. Wittmann, T. Rück, R. Bierl, F.M. Matysik, Effects of ambient parameters and cross-sensitivities from O2, CO2 and H2O on the photoacoustic detection of acetone in the UV region, Sens. Actuators, B Chem. 328 (2021), 129001.

[8] T. Rück, R. Bierl, F.M. Matysik, NO2 trace gas monitoring in air using off-beam quartz enhanced photoacoustic spectroscopy (QEPAS) and interference studies towards CO_2, H2O and acoustic noise, Sens. Actuators, B Chem. 255 (2018) 2462–2471.

[9] T. Rück, R. Bierl, F.M. Matysik, Low-cost photoacoustic NO2 trace gas monitoring at the pptV-level, Sens. Actuators, A Phys. 263 (2017) 501–509.

[10] H.A. Beck. Anwendung der Photoakustischen Spektroskopie in der Prozess- und Umweltanalytik, TU München, 2003.

[11] A. Schmohl, A. Miklós, P. Hess, Detection of ammonia by photoacoustic spectroscopy with semiconductor lasers, Appl. Opt. 41 (9) (2002) 1815–1823.

[12] R. Sussmann, W. Stremme, M. Buchwitz, R. de Beek, Validation of ENVISAT/ SCIAMACHY columnar methane by solar FTIR spectrometry at the Ground-Truthing Station Zugspitze, Atmos. Chem. Phys. 5 (9) (2005) 2419–2429.

[13] M. Phillips, R.N. Cataneo, A.R. Cummin, A.J. Gagliardi, K. Gleeson, J. Greenberg, R.A. Maxfield, W.N. Rom, Detection of lung cancer with volatile markers in the breath, Chest 123 (6) (2003) 2115–2123.

[14] C. Wang, P. Sahay, Breath analysis using laser spectroscopic techniques: breath biomarkers, spectral fingerprints, and detection limits, Sensors 9 (10) (2009) 8230–8262.

[15] J. Peltola, M. Vainio, T. Hieta, J. Uotila, S. Sinisalo, M. Metsälä, M. Siltanen, L. Halonen, High sensitivity trace gas detection by cantilever-enhanced photoacoustic spectroscopy using a mid-infrared continuous-wave optical parametric oscillator, Opt. Express 21 (8) (2013) 10240–10250.

[16] F. Mueller, A. Popp, S. Schiller, F. Kuehnemann, Cw-OPO-based photoacoustic spectrometer for highly sensitive detection of ethane and other volatile organic compounds, Photons Ultrasound.: Imaging Sens. 5320 (2004) 138.

[17] Q. Zhang, J. Chang, Z. Cong, Y. Feng, Z. Wang, F. Wang, J. Sun, Pptv-Level intra-cavity QEPAS sensor for acetylene detection using a high power Q-switched fiber laser, IEEE Sens. J. 19 (15) (2019) 6181–6186.

[18] A. Sampaolo, S. Csutak, P. Patimisco, M. Giglio, G. Menduni, V. Passaro, F.K. Tittel, M. Deffenbaugh, V. Spagnolo, Methane, ethane and propane detection using a compact quartz enhanced photoacoustic sensor and a single interband cascade laser, Sens. Actuators, B Chem. 282 (2019) 952–960.

[19] H. Zheng, M. Lou, L. Dong, H. Wu, W. Ye, X. Yin, C.S. Kim, M. Kim, W.W. Bewley, C.D. Merritt, C.L. Canedy, M.V. Warren, I. Vurgaftman, J.R. Meyer, F.K. Tittel, Compact photoacoustic module for methane detection incorporating interband cascade light emitting device, Opt. Express 25 (14) (2017) 16761–16770.

[20] H. Zheng, Y. Liu, H. Lin, R. Kan, P. Patimisco, A. Sampaolo, M. Giglio, W. Zhu, J. Yu, F.K. Tittel, V. Spagnolo, Z. Chen, Sub-ppb-level CH 4 detection by exploiting a low-noise differential photoacoustic resonator with a room-temperature interband cascade laser, Opt. Express 28 (13) (2020) 19446.

[21] H. Wu, L. Dong, X. Yin, A. Sampaolo, P. Patimisco, W. Ma, L. Zhang, W. Yin, L. Xiao, V. Spagnolo, S. Jia, Atmospheric CH4 measurement near a landfill using an ICL-based QEPAS sensor with V-T relaxation self-calibration, Sens. Actuators, B Chem. 297 (2019), 126753.

[22] K. Chen, H. Deng, M. Guo, C. Luo, S. Liu, B. Zhang, F. Ma, F. Zhu, Z. Gong, W. Peng, Q. Yu, Tube-cantilever double resonance enhanced fiber-optic photoacoustic spectrometer, Opt. Laser Technol. 123 (2020), 105894.

[23] T. Rück. Development, Characterization and Miniaturization of A Trace Gas Detection System for NO2 in Air Based on Photoacoustic Spectroscopy Dissertation, Universität Regensburg, 2017.

[24] J.-P. Besson. Photoacoustic Spectroscopy for Multi-Gas Sensing Using Near Infrared Lasers, University of Lausanne, 2006.

[27] A. Miklós, P. Hess, Z. Bozóki, Application of acoustic resonators in photoacoustic trace gas analysis and metrology, in: Rev. Sci. Instrum., 72, 2001, pp. 1937–1955.

[28] S.W. Rienstra, A. Hirschberg, An Introduction to Acoustics, 2008.

[29] J.C. Hilico, G.S. Baronov, D.K. Bronnikov, S.A. Gavrikov, I.I. Nikolaev, V. D. Rusanov, Y.G. Filimonov, High-resolution spectroscopy of (Pentad-Dyad) and (Octad-Pentad) hot bands of methan in supersonic jet, J. Mol. Spectrosc. 161 (1993) 435–444.

[30] B. Amyay, M. Louviot, O. Pirali, R. Georges, J. Vander Auwera, V. Boudon, Global analysis of the high temperature infrared emission spectrum of 12CH4 in the dyad (ν 2/ ν 4) region, J. Chem. Phys. 144 (2) (2016) 0–15.

[31] N. Barreiro, A. Vallespi, G. Santiago, V. Slezak, A. Peuriot, Influence of oxygen on the resonant photoacoustic signal from methane excited at the ν 3 mode, Appl. Phys. B Lasers Opt. 104 (4) (2011) 983–987.
[32] T.F. Hunter, D. Rumbles, M.G. Stock, The model and apparatus for the study of radiatonless processes. Photophysical Processes in the Vapour-phase measured by the optic-acoustic effect, 1973, pp. 1010–1021.
[33] S. Schlitt, J.-P. Besson, L. Thévanaz, Near-infrared laser photoacoustic detection of methane: the impact of molecular relaxation, Appl. Phys. B 82 (2005) 319–328.
[34] P. Hess, A.H. Kung, C.B. Moore, P. Hess, A.H. Kung, C.B. Moore, Vibration → vibration energy transfer in methane, J. Chem. Phys. 72 (July) (1980) 5525–5531.
[35] L. Doyennette, F. Menard-Bourcin, J. Menard, C. Boursier, C. Camy-Peyret, Vibrational energy transfer in methane excited to 2ν3 in CH4-N2/O2 mixtures from laser-induced fluorescence measurements, J. Phys. Chem. A 102 (22) (1998) 3849–3855.
[36] N. Barreiro, A. Peuriot, G. Santiago, V. Slezak, G. Santiago, GLOMAE, Water-based enhancement of the resonant photoacoustic signal from methane-air samples excited at 3.3 μm, Appl. Phys. B 108 (2012) 369–375.
[37] C. Boursier, J. Ménard, F. Ménard-Bourcin, Vibrational relaxation of methane by oxygen collisions: measurements of the near-resonant energy transfer between CH4 and O2 at low temperature, J. Phys. Chem. A 111 (30) (2007) 7022–7030.
[38] H.E. Bass, R.G. Keeton, D. Williams, Vibrational and rotational relaxation in mixtures of water vapor and oxygen, J. Acoust. Soc. Am. 60 (1) (1976) 74–77.
[39] M.H. De Vasconcelos, A.E. De Vries, Vibrational relaxation time measurements in CH4 and CH4-rare gas mixtures, Physica 86A (1977) 490–512.
[40] H.E. Bass, H.-J. Bauer, Kinetic Model for Thermal Blooming in the Atmosphere, Appl. Opt. 12 (7) (1973) 1506–1510.
[41] D.L. Huestis, Vibrational energy transfer and relaxation in O2 and H2O, J. Phys. Chem. A 110 (21) (2006) 6638–6642.

Jonas Pangerl graduated from the Applied Reserach programm, where he received his master's degree in science (M. Sc.) from the Ostbayerische Technische Hochschule (OTH) of Regensburg in Germany in 2020. Since 2018, he is a member of the Sensorik-ApplikationsZentrum (SappZ) and developed and investigated a photoacoustic trace gas sensor for hydrocarbons. Currently, Mr. Pangerl is pursuing his Doctorate of Natural Sciences (Dr. rer. nat.) in the field of human breath exhale analysis by photoacoustic spectroscopy in cooperation with the Institute for Analytical Chemistry, Chemo- and Biosensorics at the University of Regensburg in Germany.

Max Müller received his master's degree in engineering (M. Eng.) from the Ostbayerische Technische Hochschule (OTH) of Regensburg in Germany in 2020 and is currently pursuing his Doctorate of Natural Sciences (Dr. rer. nat.). Since 2018, he has been conducting research in the field of photoacoustic trace gas sensing and is focusing on vibrational energy transfer and other acoustic phenomena.

Thomas Rück studied Chemistry (Dipl. Chem.) at the University of Regensburg in Germany. In the course of his diploma thesis in cooperation with Continental Automotive GmbH, he started his research on the photoacoustic gas sensing technique in 2009. By now he has 12 years of experience in this field and received his Doctor of Science (Dr. rer. nat.) in 2017. Currently, Thomas Rück is head of the gas sensing team of the SappZ, which is affiliated to the Ostbayerische Technische Hochschule (OTH) of Regensburg.

Stefan Weigl received his master's degree in engineering (M. Eng.) from the Ostbayerische Technische Hochschule (OTH) of Regensburg in Germany in 2016 and his Doctor of Science (Dr. rer. nat.) in 2021. Both theses dealt with the research and development of photoacoustic trace gas sensing technology for environmental and medical applications. Currently, Stefan Weigl manages the four-member photoacoustic BreathSens team of the SappZ, which is located at the Ostbayerische Technische Hochschule (OTH) of Regensburg.

Rudolf Bierl became Professor at the Ostbayerische Technische Hochschule (OTH) of Regensburg and head of the SappZ in 2009. SappZ is an interdisciplinary thirty-member team mainly dealing with the investigation of various measuring principles and with the development and miniaturization of sensor systems. Mr. Bierl obtained his Diploma degree in Physics (Dipl. Phys.) from the University of Regensburg in Germany in 1991 and his Doctor of Science (Dr. rer. nat.) from the University of Erlangen in 1994. After several deployments in different sectors at Siemens VDO and Continental Automotive GmbH, he was global head of the predevelopment department of sensors at Continental from 2007 until 2009.